




Physics-Based Regularizer for Joint Soft Segmentation and Reconstruction of Electron Microscopy Images of Polycrystalline Microstructures

Amirkoushyar Ziabari , *Member, IEEE*, Jeffrey M. Rickman , Lawrence F. Drummy, Jeffrey P. Simmons, *Senior Member, IEEE*, and Charles A. Bouman , *Fellow, IEEE*

Abstract—For Bayesian image reconstruction applications in which the measured image follows from physical considerations, it is desirable to incorporate the corresponding physics into the prior model. In this paper, we use a phase-field as the physics-based prior model to implement the soft segmentation and reconstruction of noisy microstructural images of a polycrystalline, covalent material (SiC). The functional form of this prior is based on a coarse-grained Ginzburg–Landau free energy that embodies the underlying physics, and its phenomenological parameters are obtained from atomistic computer simulation. In particular, we compare an existing functional form developed by Fan and Chen for microstructural simulations with one developed here that is better suited to noise reduction in image reconstruction, and find that the latter form is indeed superior in this context. Numerical and experimental results demonstrate that the proposed method performs successful soft segmentation and reconstruction of microscopy images, even at very low signal levels. In addition, the superior performance of the proposed model for several case studies in comparison with state-of-the-art methods, such as BM3D and one using a MRF-based prior, is demonstrated.

Index Terms—Physics-based, phase-field, prior model, denoising, soft segmentation, electron microscopy, grain boundaries.

I. INTRODUCTION

SCANNING and transmission electron microscopies (SEM and TEM) are important tools for microscale/nanoscale

Manuscript received August 14, 2018; revised December 10, 2018 and January 18, 2019; accepted February 1, 2019. Date of publication February 14, 2019; date of current version November 5, 2019. This work was supported by the Materials and Manufacturing Directorate of the Air Force Research Laboratory, Dayton, OH, USA, under Contract FA8650-11-D-5800 Task Order 15. The associate editor coordinating the review of this manuscript and approving it for publication was Prof. Mathews Jacob. (*Corresponding authors: Charles A. Bouman and Amirkoushyar Ziabari.*)

A. Ziabari is with the Department of Electrical and Computer Engineering, Purdue University, IN 47907 USA (e-mail: aziabari@purdue.edu).

J. M. Rickman is with the Departments of Physics and Material Science and Engineering at Lehigh University, Bethlehem, PA 18015 USA (e-mail: jmr6@lehigh.edu).

L. F. Drummy and J. P. Simmons are with the Materials and Manufacturing Directorate, Air Force Research Laboratory, Wright-Patterson Air Force Base, OH 45433 USA (e-mail: lawrence.drummy.1@us.af.mil; jeff.simmons.3@us.af.mil).

C. A. Bouman is with the Departments of Electrical and Computer Engineering, and Biomedical Engineering at Purdue University, IN 47907 USA (e-mail: Bouman@purdue.edu).

Digital Object Identifier 10.1109/TCI.2019.2899499

characterization of materials, and novel image processing algorithms have been used to advance these techniques. In particular, image denoising algorithms are beneficial for identifying interfaces and second-phase particles from noisy microscopy images and for extracting useful properties. From a Bayesian point of view, the image prior modeling in such algorithms is especially important when the likelihood is known, and various priors including nonlocal self-similarity (NSS) models [1]–[3], sparse models [4]–[6], gradient models [7]–[9] and Markov random field (MRF) models [10]–[14] have been exploited for image denoising.

Consider first a MRF model in which a prior, defined in image space, is expressed in terms of a potential function that penalizes dissimilarities between neighboring pixels. Depending upon the choice of the potential function, a variety of MRF-based priors has been developed and employed in different image processing applications [10], [11], [15]. The correct priors can be estimated based on statistical analysis [16], [17] or from a database of natural images [8], [14], [18]. It should be noted, however, that prior models that embody only local image characteristics, and are blind to non-local behavior, have limited applicability. Thus, NSS models are popular in state-of-the-art methods such as BM3D [3], [19], LSSC [20], NCSR [5] and WNNM [21]. Finally, Sreehari *et al.* [22] developed a plug-and-play (PnP) framework [23], [24] that decouples the forward fidelity and prior terms, permitting the integration of any denoising algorithm into a prior model and thereby improving image reconstruction. Subsequently, Romano *et al.* [25] proposed a different approach, also inspired by the PnP framework, for using denoising as a prior.

The aforementioned models used priors developed without regard to the underlying processes that dictate the structures in the images. In the case of microstructural images of polycrystalline materials, for example, the geometrical features of the constituent grains (and grain boundaries) are determined by both energetic and kinetic factors. These factors are embodied in a coarse-grained description, namely a phase-field model [26], that has been used to describe grain growth and other physical phenomena, such as solidification and fluid dynamics [27], [28]. Phase-field models are in widespread use given their ability

to reproduce realistic structures in materials; thus, one expects that such a model would be a useful prior for performing image reconstruction from TEM images of materials microstructures. We note that the phase-field model has, in fact, been used in image processing applications, including segmentation, denoising [29]–[31], inpainting [32], [33] and iterative reconstruction [34]. These applications, however, used either phenomenological hyperparameters in the phase-field free energy and/or were limited to binary phases studies. For example, Sadiq *et al.* [34] used a phase-field model to perform reconstructions of tomographic imagery of metallic solidification. Their approach was limited to two-class reconstructions and did not incorporate physics directly in the estimation of nuisance parameters.

In this work, we develop a model based iterative reconstruction (MBIR) algorithm that employs a phase-field model in which the spatio-temporal evolution of a system is based on the minimization of a Ginzburg-Landau-like free energy [35]. Using a state-of-the-art phase-field model as a prior permits us to describe spatially diffuse, evolving interfaces for performing joint, soft segmentation and reconstruction from noisy images of polycrystalline microstructures. The reconstruction focuses on forming an image with continuously valued pixels, and segmentation focuses on assigning each pixel to a specific discrete class. Indeed, one novel aspect of this work is our use of an existing model of phase transitions as a regularizer. We employ the model developed by Fan and Chen [36] that uses a non-convex *bulk free energy* model, which describes phase transitions in the physical system at a coarse level, as a regularizer. In addition, we introduce a new, non-convex bulk free energy model that we call the *snap* function, and highlight its advantages in this context as compared to the Fan and Chen bulk free energy.

The resulting model constitutes a prior in the maximum-a-posteriori (MAP) estimate cost function for MBIR. For convenience, we also use a plug-and-play [24] methodology to separate the forward model from the prior model and to perform the minimization of the cost function.

We note that the forward model embodies the physics of an imaging system having Poisson noise. To minimize the corresponding cost function, a new algorithm using iterative coordinate descent (ICD) is developed. In particular, we developed a new algorithm that uses ICD along with the alternating direction method of multipliers (ADMM) [37] to minimize the constrained cost function.

As discussed below, the interfacial energy per unit area and the grain-boundary width are the key input parameters for the phase-field model, and they are obtained from atomistic simulation of a model covalent system, namely silicon carbide (SiC).

To validate our methodology, we present the results for two types of tests. In the first test, numerical phantoms are, for convenience, generated by evolving a phase-field model. We then apply the methodology to TEM images obtained with high-annular angular dark-field (HAADF) imaging.

We have selected SiC as a model experimental system for image reconstruction given its technological relevance and the importance of grain boundaries and grain triple junctions in this system in determining its functionality. In particular, SiC is an oxidation-resistant, refractory material having a relatively high hardness, and it is therefore a good candidate for

high-temperature structural materials [38]. In the case of nanocrystalline SiC having average grain sizes in the 5–20 nm range, hardness is substantially enhanced relative to the bulk due to the large fraction of grain boundaries that is inherent at the nanoscale [39], [40].

In another application that highlights the importance of grain boundaries, SiC is used to coat nuclear fuel particles and contain radionuclides produced during their use. However, radioactive Ag is found to diffuse through Ag grain boundaries, prompting detailed studies of SiC boundaries.

As relatively little is known about these boundaries, electron microscopy has been employed to interrogate the structure of individual boundaries and triple junctions and, in the presence of impurities, to characterize boundary chemistry as well [41]. Such studies have revealed the presence of distinct grain-boundary phases (known as complexions [42]) that dictate the widths of individual boundaries, where interfacial width may be inferred from Fresnel fringes in conventional TEM images of these boundaries [43]. Thus, clear images of individual grain boundaries and triple junctions in SiC are critical for characterizing material behavior.

In comparison with our conference paper [44], this work contains several new features. First, since the electron microscopy images considered here typically contain Poisson noise, we outline algorithms to describe Poisson, rather than additive Gaussian, noise. To that end, we develop a new, iterative coordinate descent algorithm with quadratic surrogates in Appendix A, and integrated this algorithm into a PnP framework with a physics-based prior. In addition, we perform joint soft segmentation and reconstruction on real high annular angular dark-field (HAADF) STEM images, as well as on several new numerical phantoms, with Poisson noise applied. Finally, and perhaps most significantly, we prove the convergence of the *snap* algorithm in Appendix B, and demonstrate why it is preferred over other non-convex, physics-based priors.

The structure of this paper is as follows. We first describe the phase-field model and the associated key equations in Section II. In Section III, we explain the procedure used to simulate microstructures. The generated microstructures are then used in Section IV to create noisy numerical phantoms. In Sections V and VI, we develop new physics-based algorithms to perform soft segmentation and reconstruction from Poisson noisy measurements. Finally, in Section VII, we demonstrate the performance of our algorithm for several numerical and real experimental case studies.

II. PHASE-FIELD MODEL

The phase-field method has been used extensively to describe and model microstructural evolution of materials [36], [45]–[48]. Unlike the Potts model, in which a continuum microstructure is mapped onto a lattice using discrete class values, the phase-field model is a description in which these discrete values are replaced by a continuous *field variable* that is associated with spatially homogenized classes [49]. The evolution of the field variables is described by the Ginzburg-Landau evolution equation [50]. In this sense, the phase-field model is a “soft-spin” model in which the *gradient penalty* associated

with the field variable leads to diffuse interfaces [27], [36] in spatially inhomogeneous systems. The Ginzburg-Landau evolution equation is described as follows.

In this work, we model a polycrystalline solid and use the word *phase* to mean the orientation of one of its p constituent grains. For this purpose, we let $\eta : \mathbb{R}^3 \rightarrow \mathbb{R}^p$ be a mapping from 3-dimensional space to a p dimensional vector in which each component corresponds to a phase in a material at a particular location. $\eta(\mathbf{r}) \in \mathbb{R}^p$ represents the phase at the location $\mathbf{r} \in \mathbb{R}^3$.

In the phase-field model, the phase field evolves according to

$$\frac{\partial \eta(\mathbf{r}, t)}{\partial t} = -L \frac{\delta F}{\delta \eta}(\mathbf{r}, t), \quad (1)$$

where L is the *relaxation coefficient* for the system, $\frac{\delta F}{\delta \eta}(\mathbf{r}, t)$ is the functional derivative of F with respect to η and F is the *total free energy functional* of the system. For convenience, we will first consider the free energy functional

$$F(\eta) = \frac{3\varepsilon}{2\sqrt{2}} \int_{\mathbb{R}^3} \left\{ \frac{1}{W_\phi} f(\eta) + \frac{W_\phi}{2} \|\nabla \eta\|^2 \right\} d^3 \mathbf{r}, \quad (2)$$

where W_ϕ is the *interface transition width* (m), ε is the *energy density of the interface* (J/m²) and $f(\eta)$ is the *bulk free energy*. Furthermore, we define $\|\nabla \eta\|^2 \equiv \sum_{i=1}^p \|\nabla \eta_i(\mathbf{r})\|^2$.

The integrand of equation (2) is composed of two terms: the bulk free energy and the *gradient energy*. The bulk free energy is generally only locally convex, allowing for multiple local minima in $F(\eta)$ and therefore multiple crystalline domains. From physical considerations, there is an energy penalty associated with an interface (due, in part, to broken bonds), the bulk free energy is balanced against the interfacial energy penalty. In a phase-field model, this interfacial energy is given by the gradient in η . Thus, the minimization of equation (2) yields the equilibrium distribution of material in the polycrystalline domains.

Fan and Chen [36] proposed a model of the bulk free energy that allowed for evolution of polycrystalline materials and is given by

$$f_{FC}(\eta(r)) = \sum_{i=1}^p \left(-\frac{1}{2} \eta_i^2(r) + \frac{1}{4} \eta_i^4(r) \right) + \sum_{i=1}^p \sum_{j \neq i}^p \eta_i^2(r) \eta_j^2(r) \quad (3)$$

III. SIMULATION OF A POLYCRYSTALLINE MICROSTRUCTURE

To generate the numerical imaging phantoms of polycrystalline microstructures, we will need to create first a microstructure using the phase-field model. The three key steps for microstructure generation are:

- 1) Discretize the phase-field evolution equation.
- 2) Compute the nuisance parameters of the phase-field model, η and W_ϕ , using atomistic simulations.
- 3) Solve the discretized evolution equation numerically.

In this section, we describe these steps and the associated generation of microstructures.

A. Discretization of the Ginzburg–Landau Evolution Equation

To effect a numerical solution, the Ginzburg-Landau equations must be discretized. This is accomplished by first redefining $\mathbf{r} = \mathbf{s} \Delta_x$ such that $\eta_{s,i} = \eta_i(\mathbf{r})$. $\eta_s \in \mathbb{R}^p$ is a p -dimensional

vector defined at each location \mathbf{s} , and each element of η_s is represented by $\eta_{s,i}$ where $i = 1, 2, \dots, p$ are indices corresponding to those elements. $\mathbf{s} = (s_1, s_2, s_3) \in \mathcal{Z}^3$ is a discrete index and Δ_x is the sample period (m). From this perspective, $\eta \in \mathbb{R}^{N \times p}$ can also be regarded as an $N \times p$ matrix.

Using the definitions above, we can rewrite the discretized version of equation (3) as follows:

$$\begin{aligned} f(\eta_s) &= \sum_{i=1}^p \left(-\frac{1}{2} \eta_{s,i}^2 + \frac{1}{4} \eta_{s,i}^4 \right) + \sum_{i=1}^p \sum_{j \neq i}^p \eta_{s,i}^2 \eta_{s,j}^2 \\ &= -\frac{1}{2} \|\eta_s\|^2 - \frac{3}{4} \|\eta_s\|_4^4 + \|\eta_s\|_4^4 \end{aligned} \quad (4)$$

where $\|\eta_s\|_P$ denotes the P -norm of η_s .

With these definitions one can approximate the total free energy by

$$\tilde{F}(\eta) \approx \frac{3\varepsilon \Delta_x^2}{2\sqrt{2}} \sum_{\mathbf{s} \in \mathcal{S}} \left\{ \frac{1}{w} f(\eta_s) + \frac{w}{2K_n} \sum_{\{r, s\} \in \mathcal{P}} \|\eta_s - \eta_r\|^2 \right\}, \quad (5)$$

where $w = \frac{W_\phi}{\Delta_x}$ is the dimensionless transition width and \mathcal{P} denotes the set of K_n nearest neighbors of \mathbf{s} i.e., $K_n = 6$ for a simple-cubic lattice.

It is also convenient to define the discrete normalized energy function

$$u(\eta) \approx \frac{1}{\gamma k_B T} \tilde{F}(\eta), \quad (6)$$

where $\gamma = \frac{3\varepsilon \Delta_x^2}{2\sqrt{2} k_B T}$.

Finally, the discretized evolution equation is given by

$$\eta^{(k+1)} = \eta^{(k)} - \rho \nabla u(\eta^{(k)}), \quad (7)$$

where $\eta^{(k)} \in \mathbb{R}^{N \times p}$ is the phase field at time $t = k \Delta_t$, where Δ_t is the time increment and $\rho = \Delta_t k_B T L / \Delta_x^3$.

B. Molecular Dynamics Atomistic Simulations

The excess interfacial energy per unit area, ε , and the width for grain boundaries, W_ϕ , are the parameters of the phase-field model.

We employed atomistic simulations of grain boundaries in silicon carbide (SiC) to estimate these parameters using a modified Tersoff potential [51]. For concreteness, we focused on twist grain boundaries at 0K temperature and calculated ε by constructing a spatially periodic unit cell and then minimizing the energy of the system by relaxing the coordinates of the constituent atoms. More specifically, we examined three twist boundaries, namely the so-called $\Sigma 5$, $\Sigma 13$ and $\Sigma 29$ boundaries [52], and found that in these cases $\varepsilon \approx 5$ J/m².

In addition, for these boundaries, we also determined the effective boundary width by calculating the planar structure factor $S(\mathbf{k})$ for a selected Bragg peak wavevectors, \mathbf{k} , lying both above and below the grain boundary plane, as shown in Figure 1 [53]. The effective interface width was obtained by fitting a hyperbolic tangent to the interfacial profile, with the result that $W_\phi \approx 0.4$ nm. It is worth noting that the structure factor can be calculated from $S(\mathbf{k}) = \sum_{l=1}^N \sum_{j=1}^N e^{i\mathbf{k}(\bar{r}_l - \bar{r}_j)}$,

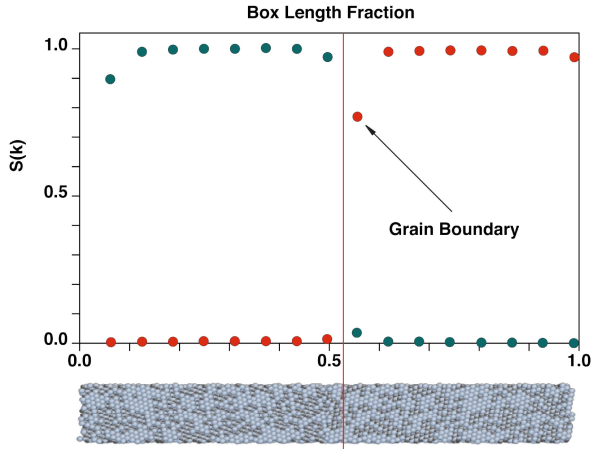


Fig. 1. The planar structure factor, $S(\mathbf{k})$, for a Bragg peak wavevector, \mathbf{k} , lying in the plane below (green points) and above (red) the grain boundary in the center of the simulation cell. The diminution of structure factor near the box length fraction of 0.5 is a reflection of the disorder induced by the boundary. The width of the boundary can be inferred from the profile near a boundary.

wherein N is the number of atoms and r is the position of each atom.

C. Numerical Solution of Ginzburg–Landau Evolution Equation

To simulate grain growth, the discretized evolution equation (7) is solved numerically using the parameters obtained from atomistic simulation in Section III-B. For ease of computation, however, it is convenient to constrain the evolving field to fall within the p -dimensional simplex set given by

$$\Omega_p = \left\{ \eta \in \mathbb{R}^p : \sum_{i=1}^p \eta_i = 1 \text{ and } \forall \eta_i \geq 0 \right\}. \quad (8)$$

This constraint may be enforced by employing the modified (discretized) evolution equation

$$\eta_s^{(k+1)} = \mathcal{P}_{\Omega_p} \left[\eta_s^{(k)} - \rho \left\{ \frac{1}{w} \nabla f(\eta_s) + \frac{w}{K_n} \sum_{r \in \partial s} (\eta_s - \eta_r) \right\} \right], \quad (9)$$

where \mathcal{P}_{Ω_p} is the operator that computes the unique projection onto the simplex set Ω_p . The operator \mathcal{P}_{Ω_p} can be computed using a finite number of iterations using Algorithm 1 [54], [55] presented below.

Algorithm 1: Projection of a p -dimensional Vector x Onto Unit Simplex. After [54], [55].

$I = \{1, 2, \dots, p\}$

Repeat

{Projection onto plane}

$$\bar{x} = \left(\sum_{i \in I} x_i \right) / |I|$$

$\forall i \in I : x_i \leftarrow x_i - \bar{x} + 1/|I|$

{Enforce inequality constraints}

$I \leftarrow I \setminus \{i : x_i < 0\}$

$\forall i \notin I : x_i \leftarrow 0$

until $\sum_{i \in I} x_i = 1$

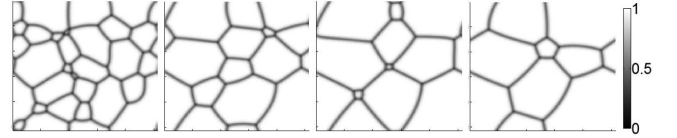


Fig. 2. The evolution of a simulated microstructure in space and time. The boundary detection function $\psi(\eta) = \sum_{i=1}^p \eta_{s,i}^2$ is plotted in each panel ($p = 16$). Each image represents a simulated image at (a) $t = 800\Delta t$, (b) $t = 2400\Delta t$, (c) $t = 4000\Delta t$, (d) $t = 7200\Delta t$, where Δt is a time step.

We solved equation (9) numerically to model grain growth, with the evolving microstructure for $p = 16$. This is shown in Figure 2. In this representation, the boundary detection function $\psi(\eta) = \sum_{s \in S, i=1}^p \eta_{s,i}^2$ is plotted in each panel, and distinct grains and delimiting grain boundaries are easily seen. For these simulations the values of the field, η , were initialized as independent, identically distributed (i.i.d) variables on $[0, 1]$, and normalized at each lattice point (pixel) within a grain to sum to unity. Each grain corresponds to a different component of the phase field vector, η .

As expected, Figure 2 evinces grain coarsening with an attendant increase in average grain size over time, and therefore a decrease in the number of grains [36]. We recorded the output microstructure at different time steps where microstructures with 11, 7, 4 and 2 grains are generated. We then used them to generate numerical phantoms with Poisson noise in Section IV.

IV. FORWARD IMAGING MODEL

In Section III, we obtained the order parameter, η , by numerically solving the evolution equation. In this section, we use the extracted η to create phantoms of microscopy images of materials. Because of the interaction of electrons with solids, the imaged intensity of a grain depends on its orientation. To first order, these intensities can be represented as a linear superposition of those due to the individual order parameters. Since $\eta \in \mathbb{R}^{N \times p}$, we define $\theta \in \mathbb{R}^p$ such that the intensity under ideal conditions of each grain is

$$x = \eta\theta.$$

Per pixel s , x represents the order parameter $\eta_s \in \mathbb{R}^p$ projected onto the single dimension of intensity ($\in \mathbb{R}$), and a measurement involves the interaction of x with the imaging system and noise.

Suppose that y represents the observed, noisy image. In imaging systems, such as electron microscopes, the observed quantity corresponds to the counts of detected electrons, which are discrete events occurring in a fixed time interval. It is known that the Poisson statistics handles discrete processes taking place in fixed time or space intervals [56]. Therefore, the probability distribution of choice here that reflects the counting statistics is a Poisson distribution [57]–[61], and each pixel intensity y_s can be modeled as a Poisson random variable.

Furthermore, we wish to estimate the rate of the Poisson variable (x). To do so, we will use a Bayesian framework, allowing this quantity to be represented by a random variable, and perform a MAP estimation of its value. Thus, the conditional

distribution of $y \in \mathbb{Z}^+$ given $x \in \mathbb{R}^+$ has the form

$$p(y|x) = \frac{x^y e^{-x}}{y!}. \quad (10)$$

Our aim, then, is to use a Bayesian framework to estimate x from measurement y . For numerical phantoms, we evaluated η from phase-field simulations, performed the mapping $x = \eta\theta$, and applied a different level of Poisson noise to x using MATLAB's *imnoise* function [62]. The phantoms were then inverted to recover the original x as a ground truth. After testing this procedure, we then apply it to real data from the SiC system (see Section VII-C).

V. MAP ESTIMATE USING ICD WITH POISSON NOISE

Given the discussion above, we can now construct a maximum-*a-posteriori* (MAP) estimate cost function and describe its minimization using iterative coordinate descent (ICD). As our focus here is on the interpretation of electron micrographs, we must first consider the nature of the measured quantities. As discussed above, the probability distribution of choice here that reflects the counting statistics for electrons is a Poisson distribution.

In order to fit within a Bayesian framework, we considered the conditional probability $p(y|x)$ for the Poisson measurement. As it is described in Appendix A, the negative log-likelihood of this conditional probability distribution can be written as

$$\ell(x) = -\log p(y|x) = -y \log x + x + \log(y!),$$

where $y \in \mathbb{Z}^+$ and $x \in \mathbb{R}^+$ denote the observed quantity (intensity) and its rate, respectively.

The MAP cost function can then be written as

$$\hat{x} = \arg \min_{x \in \mathbb{R}^+} \ell(x) + \Psi(x),$$

where $\Psi(x)$ corresponds to a general prior model and $x \in \mathbb{R}^+$ enforces the positivity constraint.

To minimize the MAP cost function, we used the ICD algorithm with a surrogate cost function. The details of the method are described in Appendix A and Algorithm 4.

VI. PLUG-AND-PLAY (PNP) FRAMEWORK WITH A PHASE-FIELD PRIOR

In the previous section we showed the general ICD algorithm for Poisson measurement, but the prior model for the MAP cost function was not discussed. In this section we discuss the phase-field prior model and develop a plug-and-play (PnP) framework that uses this prior model to minimize the cost function and obtain the map estimate.

It is worth noting that the phase-field model is remarkably similar to the Mumford-Shah potential [63] used in active contour segmentation, except that, for the latter: (1) there is a non-convex *bulk free energy* that causes partitioning between phases, and (2) it does not explicitly treat the interface region. The width of an interface and the interfacial energy are dictated by the physics of the problem. As described above, for the SiC system considered here, we estimate this width and interfacial energy from atomic-level simulations.

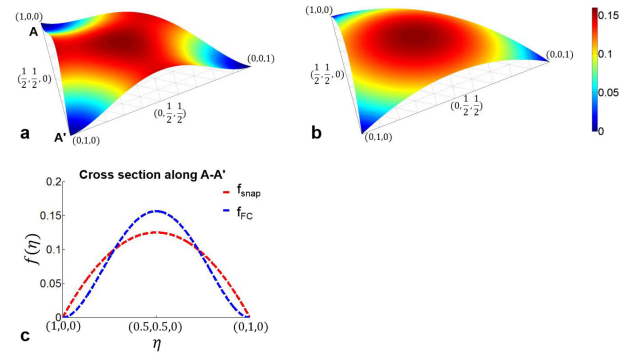


Fig. 3. A simplex plot for (a) the double-well potential ($f_{FC}(\eta)$); and (b) for the snap function ($f_{snap}(\eta)$). A constant equal to $\frac{1}{4}$ is added to original bulk free energy ($f(\eta)$) in equation 3 to offset the negative values, thereby making the energy function everywhere non-negative. (c) Comparison between cross-sections along A-A' shows the sharper vertices of the snap energy function.

A. Phase-Field Prior Model With Snap Free Energy

For phase-field regularization, the GL equation, rewritten below, will be used as a prior term to incorporate the underlying microstructural physics into image processing.

$$\tilde{F}(\eta) = c_1 \sum_{s \in S} \left(f(\eta_s) + c_2 \sum_{\{r,s\} \in \mathcal{P}} \|\eta_s - \eta_r\|^2 \right) \quad (11)$$

The first term in the sum is the bulk free energy, and the second term corresponds to an interfacial energy penalty. c_1 and c_2 are coefficients that are determined below from physical considerations.

The conventional choice for the bulk free energy, f_{η_s} is the Fan/Chen double-well potential defined in equation (4) (rewritten below).

$$f_{FC}(\eta_s) = -\frac{1}{2}\|\eta\|^2 - \frac{3}{4}\|\eta\|_4^4 + \|\eta\|^4$$

The associated simplex plot for the double-well potential energy function for $p = 3$ is shown in Figure 3a. This function is based on $f_{FC}(\eta)$, and its smoothness near the simplex vertices permits small deviations in the order parameter in response to measurements, i.e. small crystalline misorientations. The reason is that Fan and Chen's free energy, for small deviations in η from equilibrium, varies as $\|\eta\|^2$. But, well-annealed polycrystalline materials are generally sparse in orientation, so it is desirable to have a potential that behaves more like $\|\eta\|^4$.

Thus, as an alternative to the Fan and Chen free energy, we have developed the *snap potential*, which is expected to preserve sparsity more effectively. The snap function is defined by

$$f_{snap}(\eta) = \frac{5}{21}(1 - \|\eta\|^2), \quad (12)$$

where the prefactor is chosen so that $f_{snap}(\eta)$ and $f_{FC}(\eta)$ asymptotically become equivalent (in the limit of the number of phases, p). The corresponding simplex plot for the snap free energy function of order $p = 3$ is shown in Figure 3b. It should be noted that, as with $f_{FC}(\eta)$, $f_{snap}(\eta)$ also has its minima at the vertices of the simplex. However, by contrast with $f_{FC}(\eta)$, $f_{snap}(\eta)$ has sharp features and a non-vanishing derivative near

Algorithm 2: Plug-and-Play (PnP) Algorithm.

Initialize $\eta, \theta \leftarrow$ clustering of noisy measurement y
 $x = \eta\theta$
 $\hat{v} \leftarrow x \quad u \leftarrow 0$
until convergence {
 1: $\hat{x} \leftarrow \arg \min_x \sum_{s \in S} \{x_s - y_s \log(x_s) + \log(y_s!)\}$
 $+ \frac{\xi}{2} \|x - \hat{v} + u\|^2$
 2: $\tilde{v} \leftarrow \hat{x} + u$
 Denoising using A Phase-field Prior
 3: $(\hat{\eta}, \hat{\theta}) \leftarrow \arg \min_{\eta, \theta} \frac{\xi}{2} \|\tilde{v} - \eta\theta\|^2 + \Psi(\eta)$
 s.t. $\eta \in \mathbb{R}^N \times \Omega_p$
 4: $\hat{v} = \hat{\eta}\hat{\theta}$
 5: $u = u + \hat{x} - \hat{v}$

the vertices of the simplex that makes it better suited to processing noisy images. This idea is analogous to the difference between total variation and Gaussian priors in Bayesian optimization [64]. Moreover, as compared to the fourth-order free energy of f_{FC} , the quadratic free energy of f_{snap} has the virtue of greater simplicity.

B. PnP Algorithm

The PnP framework [23] provides the flexibility to mix and match the forward and the prior models of choice in Bayesian image processing and is, therefore, of great utility. Here we employ the phase-field with the snap function as the prior model. Thus, we rewrite equation (11) with the correct coefficients as follows:

$$\Psi(\eta) = \frac{\lambda}{\sigma_p} \sum_{s \in S} \left(1 - \|\eta_s\|^2 + \frac{\omega^2}{2K_n} \sum_{\{r,s\} \in \mathcal{P}} \|\eta_s - \eta_r\|^2 \right), \quad (13)$$

where $\lambda = \frac{5\gamma}{21w}$, $\omega^2 = \frac{21}{5}w^2$ and γ is defined in Section III-A. \mathcal{P} denotes the set of K_n nearest neighbors of s , and the regularization $\sigma_p = 1$.

The procedure for the PnP algorithm with the phase-field prior model is provided in Algorithm 2.

One notable difference with the standard PnP algorithm [23] is that, in the denoising step of the standard algorithm (i.e. step 3 in Algorithm 2), the cost function is minimized with respect to both η and θ , with their dot product then corresponding to the updated \hat{v} .

The minimization shown in step 3 of Algorithm 2 can be performed by the snap algorithm proposed in Algorithm 3. For this purpose, the associated cost function is then given by

$$\phi(\eta, \theta) = \frac{\xi}{2} \|\tilde{v} - \eta\theta\|^2 + \Psi(\eta) \quad \text{s.t.} \quad \eta \in \mathbb{R}^N \times \Omega_p, \quad (14)$$

The minimization procedure proposed in the snap algorithm is based on the iterative coordinate descent (ICD). We also took two further steps to enforce the constraint in equation (14). First, we enforced the positivity constraint using ADMM. The

Algorithm 3: Snap Algorithm.

Initialize $\eta, \theta \leftarrow$ clustering of noisy measurement y
 $\hat{\nu} \leftarrow \eta \quad \delta \leftarrow 0$
until convergence {
for each pixel $s \in S$ {
for k iterations {
 1: $d_s = \nabla_{\eta_s} c(\eta, \theta, \nu)$
 2: $g_s = -P_0 d_s^T$
 3: $\alpha \leftarrow \frac{\partial c(\eta_s + \alpha g_s^T, \theta, \nu)}{\partial \alpha} = 0$
 4: $\hat{\eta}_s \leftarrow \hat{\eta}_s + \alpha g_s^T$
 5: $\hat{\nu}_s \leftarrow \text{clip}(\hat{\eta}_s + \delta_s, 0)$
 6: $\delta_s \leftarrow \hat{\eta}_s - \hat{\nu}_s + \delta_s$ } }
 7: $\hat{\theta} = (\hat{\eta}^T \hat{\eta})^{-1} \hat{\eta}^T y$ }

corresponding cost function is:

$$c(\eta, \theta, \nu) = \phi(\eta, \theta) + g(\nu) + \frac{\beta}{2} \|\eta - \nu + \delta\|^2$$

$$\text{s.t.} \quad \eta \in \mathbb{R}^N \times \left\{ \eta \in \mathbb{R}^p : \sum_{i=1}^p \eta_i = 1 \right\} \quad \text{and} \quad \eta = \nu, \quad (15)$$

where $g(\nu)$ is the indicator function of the positivity set, ν and δ are ADMM auxiliary variables and $\beta > 0$ is the penalty parameter.

Next, we implemented the simplex constraint given in equation 8 by projecting the gradient into the tangent plane via the projection operator $P_0 \equiv \mathbf{I} - \frac{1}{p} \mathbf{1}\mathbf{1}^T$ [65]. In the preceding expression, \mathbf{I} is a $p \times p$ identity matrix, $\mathbf{1} \in \mathbb{R}^p$ is a vector of all ones and ν and u are the ADMM auxiliary variables employed to enforce the positivity constraint. Finally, the second step in the snap algorithm is a quadratic minimization with respect to θ (step 7 in Algorithm 3).

We should emphasize that the cost function in equation (14) is still non-convex. However, in Appendix B, we provide the conditions necessary to guarantee that the MAP negative log-likelihood is convex.

VII. RESULTS AND DISCUSSION

We used the proposed algorithm to perform soft segmentation and reconstruction from both numerical experiments and from images acquired by TEM. As described in Section III-C and IV, we used the proposed forward modeling procedure and the Ginzburg-Landau energy with the Fan/Chen bulk free energy to create binary and multiphase phantoms. The TEM data for polycrystalline SiC was obtained using the high angular annular dark-field (HAADF) microscopy technique.

A. Binary-Phase Cases

Consider first the case of a numerically-generated microstructure with two phases that has been modified with the application of Poisson noise. To quantify the microstructural noise level, it

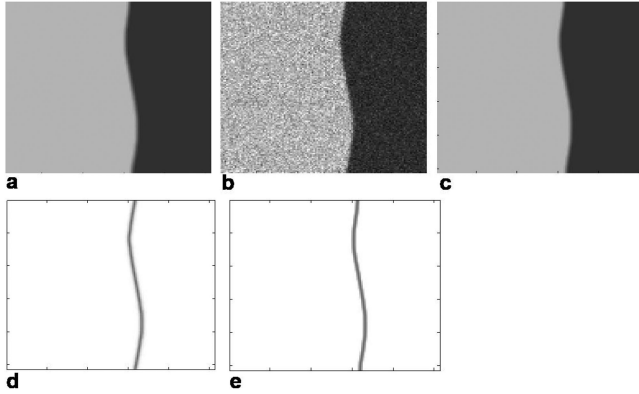


Fig. 4. Soft segmentation and reconstruction of a numerically-generated, two-phase microstructure having Poisson noise. (a) The ground truth image $x = \eta\theta$. (b) A noisy image, y , obtained by applying Poisson noise to the ground truth image (PSNR = 29.39 dB). (c) A reconstructed image $\hat{x} = \hat{\eta}\hat{\theta}$ (PSNR = 39.3 dB). (d) The ground-truth boundary detection function $\psi(\eta) = \sum_{i=1}^{p-2} \eta_{s,i}^2$. (e) The estimated order parameters ($\hat{\eta}$) plotted as $\psi(\hat{\eta})$.

is convenient to define the peak signal-to-noise ratio (PSNR)

$$PSNR \equiv 10 \log \left(\frac{x_{\max}^2}{MSE} \right),$$

where the mean-squared error

$$MSE \equiv \frac{1}{N} \sum_{i=1}^N (x(i) - (\hat{x})(i))^2.$$

Figure 4 shows the joint segmentation and reconstruction results for a binary case study. In particular, Figure 4a shows the ground truth image, while Figure 4b depicts the noisy image having a PSNR = 29.39 dB that resulted from the application of Poisson noise to the ground-truth image. To create the ground-truth image, the phase-field η obtained from the solution of the Ginzburg-Landau equations in Section III-C was employed. It was assumed that $\theta = [0.25 \ 0.75]^T$. The reconstructed image ($\hat{x} = \hat{\eta}\hat{\theta}$), shown in Figure 4c, was obtained using the snap method, that is the PnP with the snap energy function as prior, by estimating both the segmentation label matrix ($\hat{\eta}$) and the $\hat{\theta}$ matrix. It was found that the estimated $\hat{\theta} = [0.2519 \ 0.7509]^T$, which is in close agreement with the ground truth values. Finally, in Figures 4d and e, we present $\psi(\eta)$ and $\psi(\hat{\eta})$, respectively, to emphasize the accurate reconstruction of the boundary itself.

As described in Section VI-A, the snap function is employed here given its superior denoising properties relative to other plausible phase-field free energies. To demonstrate the improved performance in this context, we compared the snap and Fan/Chen priors in additional examples with different noise levels. The results are shown in Figure 5, with three separate case studies corresponding to three different noise levels shown in Figures 5a–c.

The PSNR values in Figures 5a–c are (in dB) 20.4, 9.9 and 6.9, respectively. The reconstructed images using the PnP with Fan/Chen prior are shown in Figures 5d–f and those obtained using the snap method are shown in Figures 5k–m. As the PSNR decreases, or the noise increases, the Fan/Chen prior ceases to operate appropriately and does not restore the ground truth

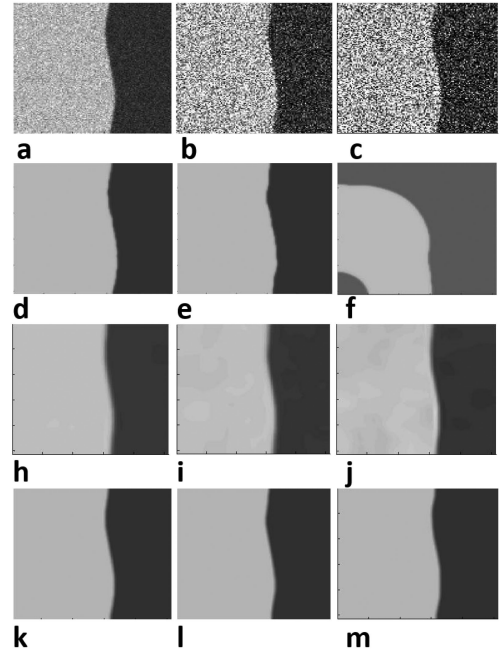


Fig. 5. Comparison between the snap method, PnP with Fan/Chen as prior and BM3D. Noisy images are shown in (a), (b), and (c). Reconstructed images using PnP with Fan/Chen as prior are in (d), (e), and (f). BM3D images are in (h), (i), and (j). Snap images are in (k), l, and (m). The PSNR values are listed in Table I.

TABLE I
PSNR VALUES (IN dB) FOR BINARY PHASE CASE STUDIES IN FIGURE 5

Noisy Image	Fan/Chen	BM3D	Snap
20.4	43.5	25	39.3
9.9	30.45	25.8	33.54
6.9	12.7	26.3	32.47

image. The PSNR for the snap images are (in dB) 39.3, 33.54 and 32.47, respectively. We conjecture that the artifact observed in Figure 5f is due to a local minimum in the free energy. This result indicates the problem in using the Fan/Chen prior in this context due to non-convexity of the cost function. Furthermore, the better performance of the PnP algorithm with the Fan/Chen prior at a relatively low noise level (Figure 5d) is attributed to the fact that the numerical phantoms are generated by solving exactly the same Fan/Chen equation. At larger noise levels, however, the non-convexity of the corresponding cost function inhibits convergence to the global minimum.

In addition, we compared the snap and Fan/chen results with the denoised images obtained using BM3D [3], [66]. The BM3D images are also shown in Figure 5. In all these cases the use of snap results in an image with a lower PSNR as compared to BM3D. The PSNR values for different cases in Figure 4 are listed in Table I. For implementation of BM3D, we used the software package provided in [66] for Poisson noise.

B. Multiphase Cases

In addition to the binary-phase cases described above, we assessed the utility of the snap algorithm to perform joint

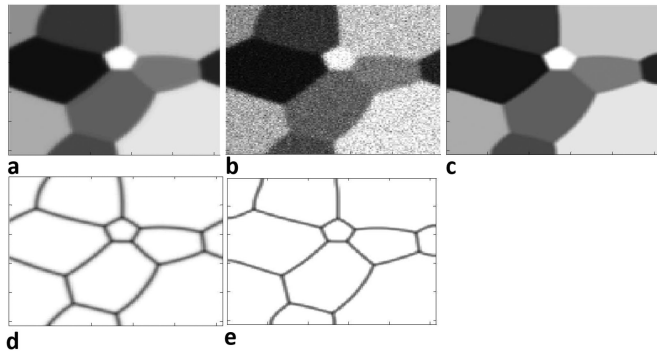


Fig. 6. Joint segmentation and reconstruction for the multiphase ($p = 11$) case study. (a) The ground truth image $x = \eta\theta$. (b) A noisy image y (PSNR = 23.25 dB). (c) The reconstructed image $\hat{x} = \hat{\eta}\hat{\theta}$ (PSNR = 36.37 dB). (d) The ground-truth order parameters (η) plotted as $\psi(\eta) = \sum_{i=1}^p \eta_{s,i}^2$. (e) The estimated order parameters ($\hat{\eta}$) plotted as $\psi(\hat{\eta})$.

TABLE II
COMPARISON BETWEEN THE GROUND TRUTH AND ESTIMATED $\hat{\theta}$

θ	θ_1	θ_2	θ_3	θ_4	θ_5	θ_6	θ_7	θ_8	θ_9	θ_{10}	θ_{11}
Ground Truth	1	2	3	4	5	6	7	8	9	10	11
Snap	1.11	2.07	3.07	3.94	5.02	6.05	7.09	7.94	8.91	9.91	11.15

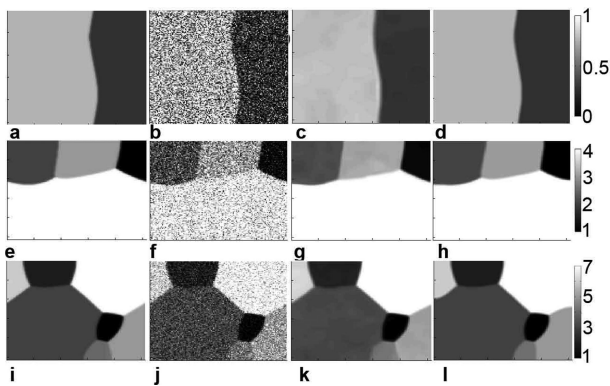


Fig. 7. Comparison between the snap and BM3D results for microstructure phantoms with different number of phases ($p = 2, 4$ and 7). Ground truth images are in: (a) $p = 2$; (e) $p = 4$; (i) $p = 7$. Noisy images are in: (b) $p = 2$; (f) $p = 4$; and (j) $p = 7$. BM3D images are in: (c) $p = 2$; (g) $p = 4$; and (k) $p = 7$. Snap images are in: (d) $p = 2$; (h) $p = 4$; and (l) $p = 7$.

segmentation and reconstruction from multiphase numerical experiments. The results of this effort are displayed in Figure 6, where Figure 6a–c show the ground truth, a noisy image and the reconstructed image using the snap method, respectively. The PSNR of the noisy image is 23.25 dB and that for the snap result is 36.37 dB. As before, the ground-truth segmentation label vector η and the estimated result are also displayed in Figure 6d and e. From these figures it can be seen that there is good agreement between the ground truth and the reconstructed images.

In addition, as it is shown in Table II, the estimated $\hat{\theta}$ values are in close agreement with the ground-truth values of θ .

We next examine the performance of the snap method for case studies with different numbers of phases. The results of this study are shown in Figure 7 for $p = 2, 4$ and 7 and in Figure 8 for $p = 11$. More specifically, Figures 7a, e, and i are the ground-truth images for these cases, while panels b, f, and j are the corresponding noisy images. (The photon counts in

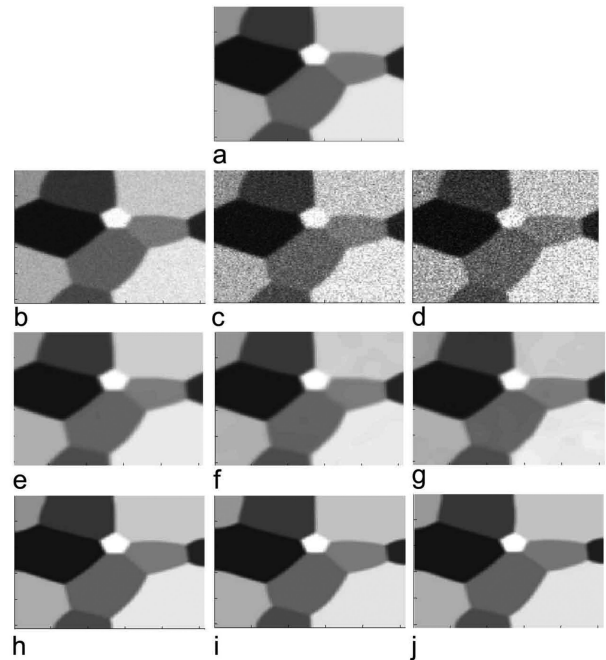


Fig. 8. Comparison between the snap and BM3D results for a multiphase case study ($p = 11$). (a) Ground-truth image. (b)–(d) Noisy images. (e)–(g) BM3D images. (h)–(j) Snap images.

TABLE III
PSNR VALUES (IN dB) FOR MULTIPHASE CASE STUDIES IN Fig. 7

p	Noisy Image	BM3D	Snap
2	6.9	26.3	32.47
4	13.5	29.3	33.9
7	18	32.2	33.3

TABLE IV
PSNR VALUES (IN dB) FOR CASE STUDY WITH $p = 11$ IN Fig. 8

Noisy Image	BM3D	Snap
33.44	35.19	38.4
23.25	34.47	36.37
20.23	35.71	31.2

all the noisy images are the same). For these different noisy images, Figures 7c, g and k are the denoised images obtained using BM3D, while panels d, h and l are obtained from the snap method. The PSNR values for BM3D and snap images are listed in Table III, which demonstrate the superior performance of snap for these cases studies.

We also compared the different noise levels with 11 phases present. This is shown in Figure 8. The noisy images are shown in Figure 8b–d, and the BM3D and snap images are shown in Figures 8e–g, and Figures 8h–j, respectively. The PSNR values are in Table IV. Based on these results, as we increase the noise, the snap method does not remain superior to BM3D for the multiphase case studies with $p = 11$ classes. In addition, compared to the ground truth images, the snap results have small artifacts at some of the interfaces. To address this issue,

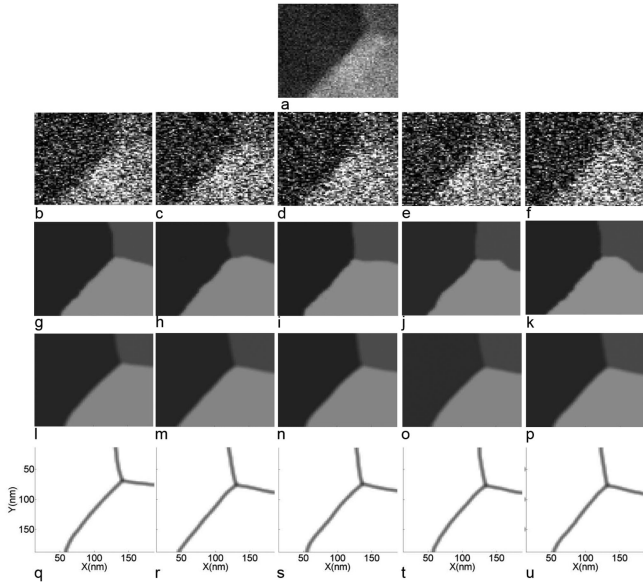


Fig. 9. Joint soft segmentation and reconstruction of noisy HAADF images of a triple junction at $1 \mu\text{s}$ dwell time. (a) HAADF images taken with $20 \mu\text{s}$ dwell time (pseudo-ground truth). (b)–(f) Noisy HAADF images with $1 \mu\text{s}$ dwell time. The average PSNR of these noisy images is 28.14 dB. Reconstructed images corresponding to (b) through (f) were obtained using: (g)–(k) the PnP algorithm with Fan/Chen prior; and, (l)–(p) the snap algorithm. (q)–(u) The estimated order parameters for each snap image in (l) through (p). ($\psi(\eta)$) are plotted which has values in $[0 1]$).

that is mainly present at larger noise levels and a larger number of grains, we may need to further optimize the regularization and physics-based parameters.

C. TEM Experiments

1) *Sample Preparation and Imaging*: A longitudinal cross section of a single silicon carbide (SiC) fiber (Tyranno SA, Ube Industries Ltd.) suitable for transmission electron microscopy (TEM) was prepared, lifted out, and welded to an OmniProbe grid using a FEI Nova Dual Beam Focused Ion Beam (DB-FIB) instrument.

Scanning transmission electron microscopy (STEM) of the fiber was done on a 300 kV FEI Titan transmission electron microscope. Data was collected in high angle (HA) dark field (DF) STEM mode using a Gatan annular DF-STEM detector with a camera length of 130 mm. Contrast in high angle annular dark-field STEM (HAADF-STEM) is related to the crystallographic orientation of the grains relative to the incident electron beam. Individual grains are approximately 200 nm in size and have a random three-dimensional crystallographic orientation distribution, or texture, in the fiber. A series of short exposure time images (20 HAADF-STEM images each with a pixel dwell time of $1 \mu\text{s}$) were taken from the same region of sample, and then a single long exposure time image (pixel dwell time of $20 \mu\text{s}$) was captured from the same region. Portions of three individual grains and three grain boundaries are visible in the Figure 9a.

2) *Results*: We used the snap method to perform joint soft segmentation and reconstruction of the HAADF-STEM images obtained for polycrystalline SiC. Since ground truths are not

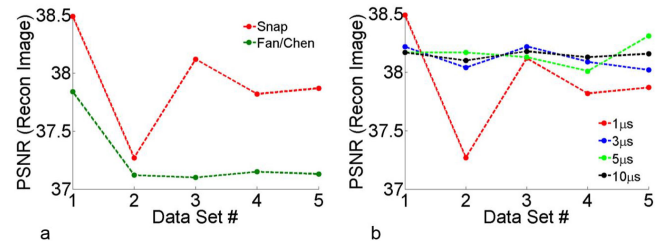


Fig. 10. (a) Comparison between the performance of the snap method and the PnP with Fan/Chen prior in terms of PSNR. Values correspond to five different cases shown in Figure 9. (b) PSNR values at different dwell times. For each dwell time, we created 5 different images (given data set number 1 to 5) and performed the reconstruction. We computed the PSNR with respect to the pseudo-ground truth at $20 \mu\text{s}$ dwell time.

available for real data, we carried out a measurement at $20 \mu\text{s}$ dwell time to obtain the *pseudo-ground truth*, and twenty DF-STEM measurements at $1 \mu\text{s}$ dwell time to obtain the noisy images.

Ideally, by averaging the twenty $1 \mu\text{s}$ images, one would expect to obtain an image with the same quality as an image obtained at $20 \mu\text{s}$ dwell time. Figure 9 shows the results for measurements numbered 1, 5, 10, 15 and 20, respectively. The pseudo-ground truth image ($20 \mu\text{s}$ dwell time) is shown in panel a. Figures 9b–f show the noisy images (all with $1 \mu\text{s}$ dwell time). The reconstructed images using PnP with the Fan/Chen prior are shown in Figures 9g–k, and those for the snap method are shown in Figures 9l–p. The PSNR values for each image were calculated with respect to the pseudo-ground truth image and plotted in Figure 10a. The red curve corresponds to the snap method and the green data points correspond to the PnP method with the Fan/Chen prior. For all of these cases, the superior performance of the snap method is evident. In Section VII-A, we showed that the use of the Fan/Chen prior in the cost function results in a non-convex optimization and we cannot guarantee its convergence. Even if using the Fan/Chen prior produces good results with real TEM images, its shortcoming in guaranteeing convergence limits its applicability. To investigate this situation further, we also estimated order parameters using the snap method. The corresponding $\psi(\eta)$ values of the estimated order parameters are plotted in Figures 9q–u. It is clear in the figures that snap recognizes the three grains and segments the results appropriately.

To analyze the performance of the snap method at different noise levels, we divided the twenty $1 \mu\text{s}$ images into groups of 3, 5 and 10 images, averaged the data in each group, and created data sets with five $3 \mu\text{s}$, $5 \mu\text{s}$, and $10 \mu\text{s}$ effective dwell time images. We performed joint segmentation and reconstruction on images in each data set, and calculated the PSNR. The calculated PSNRs are plotted in Figure 10b. These results suggest that as we increase the dwell time the consistency between the reconstructed images increases. We also compared the images in Figure 11. Figure 11a, b, c, d are the HAADF images of triple junction at $1 \mu\text{s}$, $3 \mu\text{s}$, $5 \mu\text{s}$, and $10 \mu\text{s}$ effective dwell time. PSNR values for these images are 28.3 dB, 32.2 dB, 33.7 dB, and 35.4 dB, respectively. The reconstructed images are shown

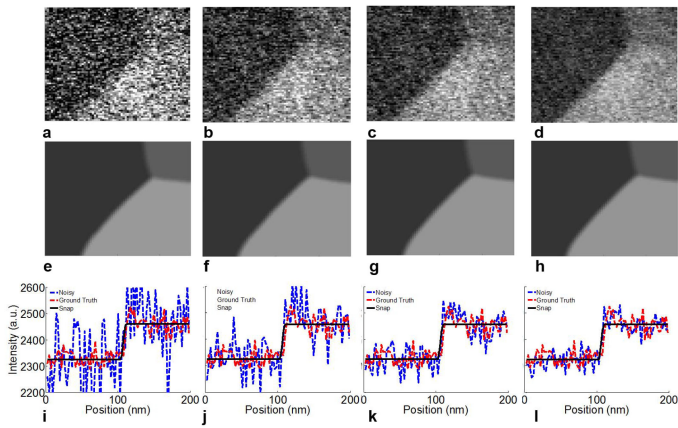


Fig. 11. Reconstruction of noisy HAADF images of a triple junction at different dwell times. Noisy HAADF images with: (a) $1 \mu\text{s}$; (b) $3 \mu\text{s}$; (c) $5 \mu\text{s}$; and (d) $10 \mu\text{s}$ dwell time. Snap images at: (e) $1 \mu\text{s}$; (f) $3 \mu\text{s}$; (g) $5 \mu\text{s}$; and (h) $10 \mu\text{s}$ dwell time. Diagonal cross section comparison between noisy (blue curve), pseudo-ground truth (red curve) and snap (black curve) results at: (i) $1 \mu\text{s}$; (j) $3 \mu\text{s}$; (k) $5 \mu\text{s}$; and (l) $10 \mu\text{s}$ dwell time. pseudo-ground truth was obtained with $20 \mu\text{s}$ dwell time (Figure 9a).

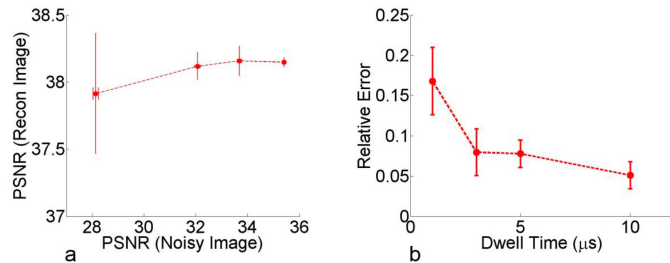


Fig. 12. Signal-to-noise and error analysis for measurements at different dwell times. (a) PSNR comparisons at different dwell times. (b) Relative error at different dwell times.

in Figure 11e, f, g, and h. It is evident that the snap algorithm can recover the grains at different noise levels. Comparison between the cross sections along the diagonal of the images are shown in Figure 11i-l.

At exposure times used in this work (1 s to 10 s in Figure 11) the noise distribution can be safely assumed Poisson. In all the cases the snap method segmented the grains correctly. For larger exposure times, beyond the experiments we performed, the noise will be weaker, and its distribution is Gaussian. The Gaussian noise is a special case for our algorithm for which the cost function will be quadratic and a surrogate function (like Appendix A) is not needed. In addition, we previously proposed a simpler version of our algorithm in [44] which can be used for Gaussian noise and can handle cases with longer exposure times and larger number of electrons. It is worth noting that, Venkatakrisnan et al. in [67] demonstrated the use and applicability of a Poisson model for HAADF-STEM imaging. The electron doses that were used to produce experimental data in our work are equal to or much lower than anything used in [67].

We carried out analysis on the segmented images in Figure 12. The average PSNR for each dataset is compared in panel a. In this figure, the x-axis corresponds to the average PSNR of

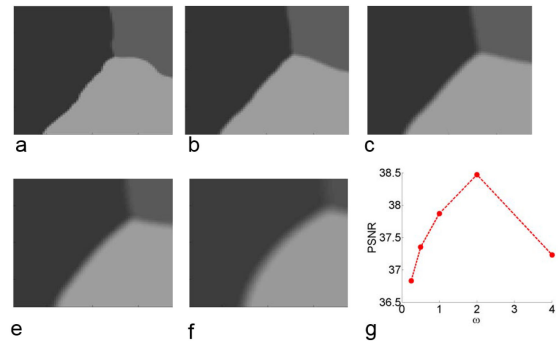


Fig. 13. Impact of changing the interface width (ω in equation (13)) on the reconstruction. As the interface width increases, the last term in equation (13) dominates the prior model (i.e., the Gaussian Markov random field (GMRF) prior). The GMRF prior over-smooths the interfaces and cannot segment the image properly.

the noisy images in the set with respect to the pseudo-ground truth image, and the y-axis present the average PSNR of the segmented images in each set.

As it is described each set in Figure 11 contains 5 images. Using these images we obtained $\binom{5}{2} = 10$ pair of images for each dataset. We then computed the root mean squared error (RMSE) for each pair. The RMSE values were then averaged (relative error) for each dataset and plotted as a function of dwell time in Figure 12b. It is evident from the figure that the relative error is decreasing as dwell time increases, suggesting a more consistent reconstruction at higher dwell time (less noisy images).

In addition, we investigated the impact of increasing interface width on the segmentation by changing ω in equation (13). This is shown in Figure 13. As we increase the interface width, the last term in equation (13) becomes the dominant term in the prior model which means we are approaching the Gaussian Markov random field (GMRF) prior. It is evident that the GMRF prior over-smooths the interfaces and cannot segment the image properly.

VIII. CONCLUSION

In this work we employed a phase-field model as a prior in a plug-and-play (PnP) framework to perform joint soft segmentation and reconstruction of noisy images of grain boundaries. In particular, we first used the Fan and Chen phase-field model [36] as a regularizer and then developed a modification of this model, which we called *snap*, to improve noise reduction and in order to assure convergence. Atomistic simulations were performed to compute phase-field model parameters consistent with the silicon carbide (SiC) system. Moreover, we developed and validated a new ICD algorithm with quadratic surrogates for denoising images having Poisson noise. Given that the phase-field model has a non-convex bulk free energy term, a method using a non-convex prior was needed. Thus, we obtained the conditions necessary to guarantee that the MAP negative log-likelihood is convex.

It was demonstrated that the snap method was able to perform joint segmentation and reconstruction of both binary

and multiphase case studies. Results for several case studies on phantoms, created by phase-field modeling, demonstrated the superior performance of the snap method as compared to the state-of-the-art image denoising algorithms. Furthermore, the snap method showed superior performance in soft segmentation and reconstruction of HAADF-STEM observations of (real) polycrystalline SiC. Consistent performance for soft segmentation and reconstruction of HAADF-STEM case studies for different exposure times (and, in turn, noise levels) were demonstrated.

ACKNOWLEDGMENT

The authors would like to acknowledge the assistance of Dr. P. Mogilevsky for contributing FIB cross sections and the extracted SiC fibers used in the experimental portion of this study. We would also like to thank Dr. N. Goel with assistance in conducting the atomistic simulations.

APPENDIX

A. ICD Optimization With Surrogate Functions for Poisson Measurement

In the case of real measurement systems, such as electron microscopes, the physical phenomena comes in discrete events. As the typical choice to accurately model process these discrete measurements, we should choose the Poisson distribution. We first start by considering the attributes of Poisson random variables. The probability mass function (PMF) of a Poisson random variable $Y \in \mathbb{Z}^+$ is given by

$$p_\lambda(y) \triangleq P_\lambda\{Y = y\} = \frac{\lambda^y e^{-\lambda}}{y!} \quad (16)$$

where $\lambda \geq 0$ represents event rate that is the average number of detected events that occur in a measurement period normalized by the detection time.

In the Bayesian framework, we will often assume that the rate of the Poisson random variable is itself random. Thus, the conditional distribution of $y \in \mathbb{Z}^+$ given $x \in \mathbb{R}^+$ has the form

$$p(y|x) = \frac{x^y e^{-x}}{y!} \quad (17)$$

We would like to use a Bayesian framework to estimate x from measurement y . From Bayes rule we have:

$$p(x|y) = \frac{p(y|x)}{p(y)} p(x) \quad (18)$$

To obtain the maximum *a posteriori* (MAP) estimate for x , we need to minimize the negative log likelihood of equation (18).

$$\begin{aligned} \hat{x}_{\text{MAP}} &= \arg \min_x (-\log p(x|y)) \\ &= \arg \min_x (-\log(p(y|x) + \log p(y) - \log p(x)) \end{aligned} \quad (19)$$

In this equation $p(y)$ is independent of x , so it can be neglected. $-\log p(x)$ is modeled by prior distribution and is discussed in the text. Here, we assume $-\log p(x) = \Psi(x)$ where $\Psi(x)$ is a general prior model.

The negative log likelihood ($-\log(p(y|x))$) and its derivative are given by the following equations.

$$\ell(x) = -\log(p(y|x)) = x - y \log x + \log(y!) \quad (20)$$

$$\ell'(x) = 1 - \frac{y}{x} \quad (21)$$

An important observation about both these functions is that they are unbounded at $x = 0$. While the negative log likelihood is convex and useful for computing a unique global minimum of corresponding MAP cost function, its form make it more difficult to deal with compared to the quadratic log likelihood as forward model. A typical approach to mitigate this problem is to use a quadratic surrogate to the negative log likelihood [68], [69].

We apply Theorem 1 to obtain the surrogate for the Poisson log likelihood in equation (20). If we assume x' as our point of approximation, then the search interval will become $x \in [x', \text{inf})$. Subsequently, the surrogate function is given by

$$q(x; x') = b(x - x') + \frac{c}{2}(x - x')^2 \quad (22)$$

where

$$b = 1 - y/x' \quad (23)$$

$$c = \frac{(b-1)x_{\min} + y}{x_{\min}(x - x_{\min})} \quad (24)$$

The Poisson log likelihood, $\ell(x)$, at $y = 1$, and its corresponding quadratic surrogates for $x' = 2$ at $x_{\min} = 0.2$ and $x_{\min} = 0.5$ are plotted in Figures 14(a) and 14(b), respectively. The larger value of $x_{\min} = 0.5$ in Figure 14(b), results in a tighter bound; however, this is at the expense of a smaller interval of $[0.5, \text{inf})$. Thus, in this case, the surrogate function is only valid for $x \geq 0.5$. When the interval is enlarged to $[0.2, \text{inf})$, then the surrogate function bound becomes looser. In general, a tighter surrogate provides a better approximation, so each update is more aggressive, and convergence is likely to be faster.

Theorem 1: surrogate for convex functions with concave derivatives

Let $f : [x_{\min}, \infty) \rightarrow \mathbb{R}$ be a convex function whose derivative $f'(x)$ is concave. Then the function

$$Q(x; x') = b(x - x') + \frac{c}{2}(x - x')^2$$

where b and c are given by

$$b = f'(x') \quad (25)$$

$$c = \frac{f'(x') - f'(x_{\min})}{x' - x_{\min}} \quad (26)$$

is a surrogate function for minimization of $f(x)$ on $x \in [x_{\min}, \text{inf})$.

While the surrogate function provides an upper bound, the selection of a value for x_{\min} remains a challenge. On solution to overcome this challenge is to make the choice of x_{\min} adaptive. To that end, we define a user selectable parameter, $0 < \gamma < 1$ and then bound the solution adaptively by setting $x_{\min} = \gamma x'$. So for example if $\gamma = 0.1$, then with each iteration of the surrogate function we can reduce the error by 90%.

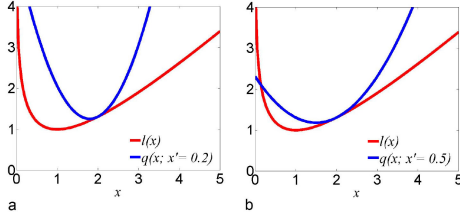


Fig. 14. Plots showing the negative log likelihood, $l(x)$, (red), and the quadratic surrogate function, $q(x; x')$, (blue) for two different values of x_{\min} . In both cases, $y = 1$ and $x' = 2$, but in (a) $x_{\min} = 0.2$ and in (b) $x_{\min} = 0.5$. Notice that the surrogate function upper bound $l(x)$ for $x \in [x_{\min}, \text{inf}]$. When $x_{\min} = 0.2$, the interval $[x_{\min}, \text{inf}]$ is larger, but the bound is looser. Alternatively, when $x_{\min} = 0.5$, the interval $[x_{\min}, \text{inf}]$ is smaller, but the bound is tighter.

Algorithm 4: ICD Algorithm for Poisson Measurement.

Initialize $0 < \gamma < 1$

Initialize $x > \mathbf{0}$

K iterations{

for each pixel $s \in S$ {

$x_{\min} \leftarrow \gamma x_s$

$b \leftarrow 1 - \frac{y_s}{x_s}$

$c \leftarrow \frac{y_s}{\gamma x_s^2}$

$x_s \leftarrow \arg \min_{\alpha \geq x_{\min}} \{b(\alpha - x_s) + \frac{c}{2}(\alpha - x_s)^2 + \Psi_i(\alpha)\}$ }

In the following we show how the surrogate function can be used to compute the MAP estimate with Poisson observations. We rewrite the MAP cost function

$$\hat{x} = \arg \min_{x \in \mathbb{R}^{+N}} \ell(x) + \Psi(x)$$

where $\Psi(x)$ corresponds to a general prior model and $x \in \mathbb{R}^{+N}$ enforces the positivity constraint.

To minimize the MAP estimate, we use the ICD algorithm. The ICD update for the s^{th} pixel is given by

$$\hat{x}_s \leftarrow \arg \min_{\alpha \geq 0} \ell_s(\alpha) + \Psi_s(\alpha),$$

where

$$\ell_s(\alpha) = \alpha - y_s \log(\alpha) + \log(y_s!).$$

We can then define a quadratic surrogate function

$$q_s(\alpha; x') = b(\alpha - x') + \frac{c}{2}(\alpha - x')^2,$$

where x' is the pixel's initial value.

The ICD update then becomes

$$\hat{x}_s \leftarrow \arg \min_{\alpha \geq 0} q_s(\alpha; x') + \Psi_s(\alpha),$$

As already discussed, we set $x_{\min} = \gamma x'$. Typically, one might select $0.1 \leq \gamma \leq 0.25$. Next, we compute coefficients b and c , from equations (23) and (24):

$$b = 1 - y/x' \quad (27)$$

$$c = \frac{y}{\gamma x_s'^2} \quad (28)$$

Putting this all together results in the ICD update Algorithm 4.

B. Discussion of Convergence

In Algorithm 2 and 3, we discussed the PnP algorithm. The algorithm has two parts. While in the first part we minimize a strictly convex function, in the second part the function is not convex. The non-convexity of the bulk free energy is a characteristic of the Landau Theory of Phase Transitions [35]. A phase transition occurs when a non-convexity in the bulk free energy develops, leading to multiple degenerate solutions to $\{\eta \in \mathbb{R}^p : \eta = \arg \min_{\eta} f(\eta)\}$. In the case of polycrystalline materials, typically, they formed as a phase transition from a liquid phase because of this non-convexity. This is a novel innovation in this work that we use an existing theory of phase transitions for a regularizer. However, non-convex regularizers need to be manipulated in order to make the whole expression convex, for which the procedure is described in the following.

Below we write a simplified version of the second cost function in the PnP algorithm that needs to be minimized at a single pixel $s \in S$.

$$\begin{aligned} \hat{\eta}_s \leftarrow \arg \min_{\eta_s} c(\eta_s) &= \frac{\xi}{2} \|\tilde{v}_s - \eta_s \theta\|^2 + \frac{\alpha}{2} (1 - \|\eta_s\|^2) \\ &+ \frac{\beta}{2} \|\eta_s - \nu_s + \delta_s\|^2 + \frac{\zeta}{2} \sum_{\{r,s\} \in \mathcal{P}} \|\eta_s - \eta_r\|^2 \end{aligned}$$

$$\text{s.t. } \eta_s \in \left\{ \eta_s \in \mathbb{R}^p : \sum_{i=1}^p \eta_{s,i} = 1 \right\} \quad \text{and} \quad \eta_s = \nu_s \quad (29)$$

where ξ, α, β and ζ are hypothetical coefficients that are all positive and should be replaced by the original parameters/coefficients from the equations in the main text ($\xi, \alpha = \frac{2\lambda}{\sigma_p}, \beta$ and $\zeta = \frac{\lambda\omega^2}{\sigma_p K_n}$). \tilde{v}_s is the output of the first step of the PnP Algorithm 2 at pixel $s \in S$, and ν_s and δ are ADMM auxiliary variables to enforce positivity.

Here we would like to discuss the convergence of this cost function. It is evident that only the second term will cause trouble for convergence of the cost function as it is unbounded concave function of η_s . The third term was added to enforce the positivity constraint using variables ν_s and δ_s in ADMM algorithm. Intuitively, by choosing a large value for coefficient β , we expect the cost function always remain convex with its minima at the vertices of simplex.

To further study the convergence theoretically, and understand impacts of different coefficients, we assumed the following case with: $\tilde{v}_s \in \mathbb{R}, p = 2, \eta_s = [\eta_{s,1} \ \eta_{s,2}] \in \mathbb{R}^p$, and $\theta = [\theta_1 \ \theta_2] \in \mathbb{R}^p$.

With these assumptions in mind, the Hessian of the cost function, H , can be written as:

$$\begin{aligned} H &= \begin{bmatrix} \frac{\partial^2 c}{\eta_{s,1}^2} & \frac{\partial^2 c}{\eta_{s,1}\eta_{s,2}} \\ \frac{\partial^2 c}{\eta_{s,2}\eta_{s,1}} & \frac{\partial^2 c}{\eta_{s,2}^2} \end{bmatrix} \\ &= \begin{bmatrix} \xi\theta_1^2 - \alpha + \beta + \zeta & \xi\theta_1\theta_2 \\ \xi\theta_1\theta_2 & \xi\theta_2^2 - \alpha + \beta + \zeta \end{bmatrix} \end{aligned}$$

For the cost function to become convex, the eigenvalues of the H must be positive so that the Hessian becomes positive definite.

The eigenvalues $\chi = [\chi_1 \ \chi_2]$ can be obtained from the following equation:

$$\det(H - \chi \mathbf{I}) = 0$$

Thus, we get:

$$\chi^2 - \xi(\|\theta\|^2 - 2r)\chi + (r^2 - \xi r\|\theta\|^2) = 0 \quad (30)$$

where we assumed $r = \alpha - (\beta + \zeta)$.

By computing the discriminant of the quadratic equation, Δ , it can easily be shown that the equation 30 has always two real roots.

$$\begin{aligned} \Delta &= \xi^2\|\theta\|_2^4 - 4r\xi\|\theta\|_2^2 + 4r^2 - 4r^2 + 4r\xi\|\theta\|_2^2 \\ &= \xi^2\|\theta\|_2^4 > 0 \end{aligned}$$

Also, for those roots to be positive we must have:

$$\xi\|\theta\|^2 - 2(\alpha - (\beta + \zeta)) > 0$$

If we replace $\xi = 1$, $\alpha = \frac{2\lambda}{\sigma_p}$, β and $\zeta = \frac{\lambda\omega^2}{\sigma_p K_n}$ from the text we have:

$$\sigma_p(\|\theta\|^2 + \beta) - 2\lambda \left(2 - \frac{\omega^2}{K_n}\right) > 0 \quad (31)$$

It is clear that by choosing β and/or σ_p very large we can guarantee positive eigenvalues. However, large regularization parameter σ_p will cause the impact of prior to be diminished and therefore, one should pay attention in choosing that parameter.

REFERENCES

- [1] A. Buades, B. Coll, and J.-M. Morel, "Non-Local means denoising," *Image Process. Line*, vol. 1, pp. 490–530, 2011.
- [2] A. Buades, B. Coll, and J.-M. Morel, "A non-local algorithm for image denoising," in *Proc. IEEE Comput. Soc. Conf. Comput. Vision Pattern Recognit.*, 2005, vol. 2, pp. 60–65.
- [3] K. Dabov, A. Foi, and K. Egiazarian, "Video denoising by sparse 3D transform-domain collaborative filtering," *Eur. Signal Process. Conf.*, vol. 16, no. 8, pp. 145–149, 2007.
- [4] M. Elad and M. Aharon, "Image denoising via sparse and redundant representations over learned dictionaries," *IEEE Trans. Image Process.*, vol. 15, no. 12, pp. 3736–3745, Dec. 2006.
- [5] W. Dong, L. Zhang, G. Shi, and X. Li, "Nonlocally centralized sparse representation for image restoration," *IEEE Trans. Image Process.*, vol. 22, no. 4, pp. 1620–1630, Apr. 2013.
- [6] M. Aharon, M. Elad, and A. Bruckstein, "K-SVD: An algorithm for designing overcomplete dictionaries for sparse representation," *IEEE Trans. Signal Process.*, vol. 54, no. 11, pp. 4311–4322, Nov. 2006.
- [7] L. I. Rudin, S. Osher, and E. Fatemi, "Nonlinear total variation based noise removal algorithms," *Physica D: Nonlinear Phenom.*, vol. 60, no. 1–4, pp. 259–268, 1992.
- [8] Y. Weiss and W. T. Freeman, "What makes a good model of natural images?," in *Proc. IEEE Comput. Vision Pattern Recognit.*, 2007, pp. 1–8.
- [9] S. Osher, M. Burger, D. Goldfarb, J. Xu, and W. Yin, "An iterative regularization method for total variation-based image restoration," *Multiscale Model. Simul.*, vol. 4, no. 2, pp. 460–489, 2005.
- [10] D. Geman and G. Reynolds, "Constrained restoration and the recovery of discontinuities," *IEEE Trans. Pattern Anal. Mach. Intell.*, vol. 14, no. 3, pp. 367–383, Mar. 1992.
- [11] C. A. Bouman and K. D. Sauer, "A generalized Gaussian image model for edge-preserving MAP estimation," *IEEE Trans. Image Process.*, vol. 2, no. 3, pp. 296–310, Jul. 1993.
- [12] F. Li, C. Shen, and C. Li, "Multiphase soft segmentation with total variation and H1 regularization," *J. Math. Imaging Vision*, vol. 37, no. 2, pp. 98–111, 2010.
- [13] X. Lan, S. Roth, D. Huttenlocher, and M. J. Black, "Efficient belief propagation with learned higher-order Markov random fields," in *Proc. Eur. Conf. Comput. Vision*, 2006, pp. 269–282.
- [14] S. Roth and M. J. Black, "Fields of experts: A framework for learning image priors," in *Proc. Comput. Vision Pattern Recognit.*, 2005, vol. 2, pp. 860–867.
- [15] J.-B. Thibault, K. D. Sauer, C. A. Bouman, and J. Hsieh, "A three-dimensional statistical approach to improved image quality for multislice helical CT," *Med. Phys.*, vol. 34, no. 11, pp. 4526–4544, 2007.
- [16] S. Geman and D. Geman, "Stochastic relaxation, Gibbs distributions, and the Bayesian restoration of images," *IEEE Trans. Pattern Anal. Mach. Intell.*, vol. PAMI-6, no. 6, pp. 721–741, Nov. 1984.
- [17] S. S. Saquib, C. A. Bouman, and K. Sauer, "ML parameter estimation for Markov random fields with applications to Bayesian tomography," *IEEE Trans. Image Process.*, vol. 7, no. 7, pp. 1029–1044, Jul. 1998.
- [18] M. F. Tappen, C. Liu, E. H. Adelson, and W. T. Freeman, "Learning Gaussian conditional random fields for low-level vision," in *Proc. IEEE Comput. Vision Pattern Recognit.*, 2007, pp. 1–8.
- [19] K. Dabov, A. Foi, V. Katkovnik, and K. Egiazarian, "BM3D image denoising with shape-adaptive principal component analysis," in *Proc. SPARS'09—Signal Process. Adapt. Sparse Structured Represent.*, 2009, pp. 1–6.
- [20] J. Mairal, F. Bach, J. Ponce, G. Sapiro, and A. Zisserman, "Non-local sparse models for image restoration," in *Proc. IEEE 12th Int. Conf. Comput. Vision*, 2009, pp. 2272–2279.
- [21] S. Gu, L. Zhang, W. Zuo, and X. Feng, "Weighted nuclear norm minimization with application to image denoising," in *Proc. IEEE Conf. Comput. Vision Pattern Recognit.*, 2014, pp. 2862–2869.
- [22] S. Sreehari, S. V. Venkatakrisnan, L. F. Drummy, J. P. Simmons, and C. A. Bouman, "Advanced prior modeling for 3D bright field electron tomography," *Proc. SPIE*, 2015, Art. no. 940108.
- [23] S. V. Venkatakrisnan, C. A. Bouman, and B. Wohlberg, "Plug-and-play priors for model based reconstruction," in *Proc. IEEE Global Conf. Signal Inf. Process.*, 2013, pp. 945–948.
- [24] S. Sreehari *et al.*, "Plug-and-play priors for bright field electron tomography and sparse interpolation," *IEEE Trans. Comput. Imaging*, vol. 2, no. 4, pp. 408–423, Dec. 2016.
- [25] Y. Romano, M. Elad, and P. Milanfar, "The little engine that could: Regularization by denoising (red)," *SIAM J. Imaging Sci.*, vol. 10, no. 4, pp. 1804–1844, 2017.
- [26] J. D. Gunton and M. Droz, *Introduction*, vol. 183 of *Lecture Notes in Physics*, Berlin Springer Verlag, Springer, 1983.
- [27] I. Steinbach, "Phase-field models in materials science," *Model. Simul. Mater. Sci. Eng.*, vol. 17, no. 7, 2009, Art. no. 073001.
- [28] L.-Q. Chen, "Phase-field models for microstructure evolution," *Annu. Rev. Mater. Res.*, vol. 32, no. 1, pp. 113–140, 2002.
- [29] C. A. Z. Barcelos, Y. Chen, and F. Chen, "Soft image segmentation based on the mixture of Gaussians and the phase-transition theory," *Appl. Math.*, vol. 5, pp. 2888–2898, 2014.
- [30] A. Lauric and S. Frisken, "Soft segmentation of CT brain data," Dept. Comput. Sci., Tufts Univ., Medford, MA, USA, Tech. Rep. TR-2007–3, 2007.
- [31] T. Preusser, M. Droske, C. S. Garbe, A. Telea, and M. Rumpf, "A phase field method for joint denoising, edge detection, and motion estimation in image sequence processing," *SIAM J. Appl. Math.*, vol. 68, no. 3, pp. 599–618, 2007.
- [32] J. A. Dobrosotskaya and A. L. Bertozzi, "Analysis of the wavelet Ginzburg–Landau energy in image applications with edges," *SIAM J. Imaging Sci.*, vol. 6, no. 1, pp. 698–729, 2013.
- [33] A. Gillette, "Image inpainting using a modified Cahn–Hilliard equation," Ph.D. dissertation, Dept. Math., Univ. California Los Angeles, Los Angeles, CA, USA, 2006.
- [34] M. U. Sadiq, J. P. Simmons, and C. A. Bouman, "Model based image reconstruction with physics based priors," in *Proc. IEEE Int. Conf. Image Process.*, 2016, pp. 3176–3179.
- [35] L. D. Landau and E. M. Lifshitz, *Statistical Physics: Volume 5 (Course of Theoretical Physics, Volume 5)*. New York, NY, USA: Elsevier, 1980.
- [36] D. Fan and L.-Q. Chen, "Computer simulation of grain growth using a continuum field model," *Acta Materialia*, vol. 45, no. 2, pp. 611–622, 1997.
- [37] C. A. Bouman, *Model Based Image Processing*, 2019. [Online]. Available: <https://engineering.purdue.edu/~bouman/publications/pdf/MBIP-book.pdf>

- [38] K. Yamada and M. Mohri, "Properties and applications of silicon carbide ceramics," in *Silicon Carbide Ceramics—1*. New York, NY, USA: Springer-Verlag, 1991, pp. 13–44.
- [39] F. Gao, D. Chen, W. Hu, and W. J. Weber, "Energy dissipation and defect generation in nanocrystalline silicon carbide," *Phys. Rev. B*, vol. 81, no. 18, 2010, Art. no. 184101.
- [40] F. Liao, S. L. Girshick, W. M. Mook, W. W. Gerberich, and M. R. Zachariah, "Superhard nanocrystalline silicon carbide films," *Appl. Phys. Lett.*, vol. 86, no. 17, 2005, Art. no. 171913.
- [41] F. Cancino-Trejo, D. J. Navarro-Solis, E. López-Honorato, J. Rabone, R. C. Walker, and R. Salomon, "Grain boundary complexions in silicon carbide," *J. Amer. Ceram. Soc.*, vol. 101, no. 3, pp. 1009–1013, 2018.
- [42] P. R. Cantwell, M. Tang, S. J. Dillon, J. Luo, G. S. Rohrer, and M. P. Harmer, "Grain boundary complexions," *Acta Materialia*, vol. 62, pp. 1–48, 2014.
- [43] H.-J. Kleebe, "Comparison between SEM and TEM imaging techniques to determine grain-boundary wetting in ceramic polycrystals," *J. Amer. Ceram. Soc.*, vol. 85, no. 1, pp. 43–48, 2002.
- [44] A. Ziabari, J. Rickman, J. Simmons, and C. A. Bouman, "Physics based modeling for the development of soft segmentation and reconstruction algorithms," in *Proc. 51st Asilomar Signal, Syst. Comput.*, 2017, pp. 1875–1880.
- [45] N. Moelans, B. Blanpain, and P. Wollants, "An introduction to phase-field modeling of microstructure evolution," *Calphad*, vol. 32, no. 2, pp. 268–294, 2008.
- [46] S. Y. Hu and L. Q. Chen, "A phase-field model for evolving microstructures with strong elastic inhomogeneity," *Acta Materialia*, vol. 49, no. 11, pp. 1879–1890, 2001.
- [47] N. Provatas *et al.*, "Using the phase-field crystal method in the multi-scale modeling of microstructure evolution," *J. Minerals, Metals Mater. Soc.*, vol. 59, no. 7, pp. 83–90, 2007.
- [48] L. Q. Chen and J. Shen, "Applications of semi-implicit fourier-spectral method to phase field equations," *Comput. Phys. Commun.*, vol. 108, no. 2/3, pp. 147–158, 1998.
- [49] V. Tikare, E. A. Holm, D. Fan, and L.-Q. Chen, "Comparison of phase-field and Potts models for coarsening processes," *Acta Materialia*, vol. 47, no. 1, pp. 363–371, 1998.
- [50] P. C. Hohenberg and B. I. Halperin, "Theory of dynamic critical phenomena," *Rev. Mod. Phys.*, vol. 49, no. 3, 1977, Art. no. 435.
- [51] N. Goel, E. B. Webb III, A. Oztekin, J. M. Rickman, and S. Neti, "Kapitza resistance at segregated boundaries in β -sic," *J. Appl. Phys.*, vol. 118, no. 11, 2015, Art. no. 115101.
- [52] V. Randle, *The Measurement of Grain Boundary Geometry*, Evanston, IL, USA: Routledge, 2017.
- [53] P. M. Chaikin, T. C. Lubensky, and T. A. Witten, *Principles of Condensed Matter Physics*, vol. 1, Cambridge, U.K.: Cambridge Univ. Press, 1995.
- [54] C. Michelot, "A finite algorithm for finding the projection of a point onto the canonical simplex of ∞_n ," *J. Optim. Theory Appl.*, vol. 50, no. 1, pp. 195–200, 1986.
- [55] C. Zach, D. Gallup, J.-M. Frahm, and M. Niethammer, "Fast global labeling for real-time stereo using multiple plane sweeps," in *Vision, Modeling, and Visualization*, Amsterdam, The Netherlands: IOS Press, 2008, pp. 243–252.
- [56] D. C. Joy, *Noise and its Effects on the Low-Voltage SEM*. New York, NY, USA: Springer-Verlag, 2008, pp. 129–144.
- [57] S. W. Hasinoff, "Photon, Poisson noise," in *Computer Vision*. New York, NY, USA: Springer-Verlag, 2014, pp. 608–610.
- [58] A. Tejada and J. den Dekker Arnold, "The role of Poisson's binomial distribution in the analysis of TEM images," *Ultramicroscopy*, vol. 111, no. 11, pp. 1553–1556, 2011.
- [59] N. Mevenkamp, P. Binev, W. Dahmen, P. M. Voyles, A. B. Yankovich, and B. Berkels, "Poisson noise removal from high-resolution stem images based on periodic block matching," in *Advanced Structural Chemical Imaging*. New York, NY, USA: Springer-Verlag, 2015.
- [60] N. Mevenkamp, A. B. Yankovich, P. M. Voyles, and B. Berkels, "Non-local means for scanning transmission electron microscopy images and Poisson noise based on adaptive periodic similarity search and patch regularization," in *Proc. Vision Model. Vis.*, 2014, pp. 63–70.
- [61] S. Venkatakrisnan, L. Drummy, M. Jackson, M. de Graef, J. Simmons, and C. Bouman, "Bayesian tomographic reconstruction for high angle annular dark field (HAADF) scanning transmission electron microscopy (STEM)," in *Proc. IEEE Statist. Signal Process. Workshop*, 2012, pp. 680–683.
- [62] MATLAB Release 2016, The MathWorks, Inc., Natick, Massachusetts, MA, USA.
- [63] D. Mumford and J. Shah, "Optimal approximations by piecewise smooth functions and associated variational problems," *Commun. Pure Appl. Math.*, vol. 42, no. 5, pp. 577–685, 1989.
- [64] K. Sauer and C. Bouman, "Bayesian estimation of transmission tomograms using segmentation based optimization," *IEEE Trans. Nucl. Sci.*, vol. 39, no. 4, pp. 1144–1152, Aug. 1992.
- [65] H. Garcke and B. Nestler, "A mathematical model for grain growth in thin metallic films," *Math. Models Methods Appl. Sci.*, vol. 10, no. 06, pp. 895–921, 2000.
- [66] L. Azzari and A. Foi, "Variance stabilization for noisy+estimate combination in iterative Poisson denoising," *IEEE Signal Process. Lett.*, vol. 23, no. 8, pp. 1086–1090, Aug. 2016.
- [67] S. V. Venkatakrisnan, L. F. Drummy, M. A. Jackson, M. de Graef, J. Simmons, and C. A. Bouman, "A model based iterative reconstruction algorithm for high angle annular dark field-scanning transmission electron microscope (HAADF-STEM) tomography," *IEEE Trans. Image Process.*, vol. 22, no. 11, pp. 4532–4544, Nov. 2013.
- [68] J. Zheng, S. S. Saquib, K. Sauer, and C. A. Bouman, "Parallelizable Bayesian tomography algorithms with rapid, guaranteed convergence," *IEEE Trans. Image Process.*, vol. 9, no. 10, pp. 1745–1759, Oct. 2000.
- [69] Z. Yu, J. B. Thibault, C. A. Bouman, K. D. Sauer, and J. Hsieh, "Fast model-based X-ray CT reconstruction using spatially nonhomogeneous ICD optimization," *IEEE Trans. Image Process.*, vol. 20, no. 1, pp. 161–175, Jan. 2011.



Amirkoushyar Ziabari received the Ph.D. degree from the Department of ECE, Purdue University, IN, USA, in 2016. He is a Postdoctoral Research Associate with the Imaging, Signals and Machine Learning (IS&ML) Group, Oak Ridge National Laboratory (ORNL), Oak Ridge, TN, USA. Before joining the ORNL, he was a Postdoc with the Integrated Imaging Group, Department of Electrical and Computer Engineering (ECE), Purdue University. His research interests are at the intersection of physics, signal processing, and machine learning, where he has used

image/signal processing and machine learning ideas to explore multiscale experimental physics phenomena. He is currently working on data analytic, data driven and physics-based image reconstruction and segmentation for advanced manufacturing in order to improve the state-of-the-art in real time monitoring of the process.



Jeffrey M. Rickman joined Lehigh University, Bethlehem, PA, USA, in 1993 after postdoctoral appointments with the University of Michigan and Argonne National Laboratory. He holds a joint appointment with the Departments of Physics and the Department of Materials Science and Engineering at the Lehigh University. His research interests include the development of computer simulation methodologies for describing fluids and solids, the determination of the elastic properties of defects, the kinetics of phase transformations, and materials informatics. He is the

recipient of several honors including the Young Investigator Award from the National Science Foundation, the Chambers Junior Professorship, and the Culler Prize (Miami University).



Lawrence F. Drummy received the B.S. degree in physics from Rensselaer Polytechnic Institute, Troy, NY, USA, in 1998, while developing image processing tools for scanning tunneling microscopy, and the Ph.D. degree from the Department of Materials Science and Engineering, University of Michigan, Ann Arbor, MI, USA, in 2003, while performing research on flexible electronic materials. He is a Materials Engineer with the Soft Matter Materials Branch, Functional Materials Division, Materials and Manufacturing Directorate, Air Force Research Laboratory,

Dayton, OH, USA. His research interests include tomography and inverse problems, signal and image processing, high-resolution transmission electron microscopy, nanocomposites, organic/inorganic interfaces, structural proteins, metamaterials, and organic electronics.



Jeffrey P. Simmons received the B.S. degree in metallurgical engineering from the New Mexico Institute of Mining and Technology, Socorro, NM, USA, in 1983, the M.E. degree in metallurgical engineering and materials science and the Ph.D. degree in materials science and engineering from Carnegie Mellon University, Pittsburgh, PA, USA, in 1985 and 1992, respectively. He is currently a Materials and Imaging Scientist with the Metals Branch, Materials and Manufacturing Directorate of the Air Force Research Laboratory, OH, USA. He is currently involved in

developing mathematical algorithms for the data analysis of emerging large digital datasets produced by advances in microscope characterization capabilities.



Charles A. Bouman received the B.S.E.E. degree from the University of Pennsylvania, Philadelphia, PA, USA, in 1981, and the M.S. degree from the University of California at Berkeley, Berkeley, CA, USA, in 1982, and the Ph.D. degree in electrical engineering from Princeton University, Princeton, NJ, USA, in 1989. From 1982 to 1985, he was a Full Staff Member with the MIT Lincoln Laboratory. In 1989, as a Faculty, he joined the Purdue University, West Lafayette, IN, USA, where he is currently the Showalter Professor of electrical and computer engineering

and biomedical engineering. His research interests include statistical signal and image processing in applications ranging from medical to scientific and consumer imaging. His research resulted in the first commercial model-based iterative reconstruction (MBIR) system for medical X-ray computed tomography, and he is the Co-Inventor for more than 50 issued patents that have been licensed and used in millions of consumer imaging products. He is the recipient of the 2014 Electronic Imaging Scientist of the Year Award and the IS&Ts Raymond C. Bowman Award. He has been a Purdue University Faculty Scholar and was the recipient of the College of Engineering Engagement/Service Award and Team Award. He was also a Founding Co-Director of Purdues Magnetic Resonance Imaging Facility from 2007 to 2016 and the Chair of Purdues Integrated Imaging Cluster from 2012 to 2016. He was the Editor-in-Chief for the IEEE TRANSACTIONS ON IMAGE PROCESSING, a Distinguished Lecturer for the IEEE Signal Processing Society, and a Vice President of Technical Activities for the IEEE Signal Processing Society, during which time he lead the creation of the IEEE TRANSACTIONS ON COMPUTATIONAL IMAGING. He has been an Associate Editor for the IEEE TRANSACTIONS ON IMAGE PROCESSING, the IEEE TRANSACTIONS ON PATTERN ANALYSIS AND MACHINE INTELLIGENCE, and the *SIAM Journal on Mathematical Imaging*. He has also been a Vice President of Publications and a Member of the Board of Directors for the Imaging Science and Technology (IS&T) Society. He is the Founder and Co-Chair of the SPIE/IS&T Conference on Computational Imaging. He is a Member of the National Academy of Inventors, a Fellow of the American Institute for Medical and Biological Engineering (AIMBE), a Fellow of the Society for the IS&T, and a Fellow of the SPIE Professional Society.